

Thermal ionization and thermally activated crossover quenching processes for $5d$ - $4f$ luminescence in $\text{Y}_3\text{Al}_{5-x}\text{Ga}_x\text{O}_{12} : \text{Pr}^{3+}$

Jumpei Ueda,^{1,2,3,4,*} Andries Meijerink,⁴ Pieter Dorenbos,³ Adrie J. J. Bos,³ and Setsuhisa Tanabe¹

¹Graduate School of Human and Environmental Studies, Kyoto University, Kyoto 606-8501, Japan

²Graduate School of Global Environmental Studies, Kyoto University, Kyoto 606-8501, Japan

³Luminescence Materials Research Group, Section FAME-RST, Faculty of Applied Sciences, Delft University of Technology, 2629 JB Delft, Netherlands

⁴Debye Institute, Utrecht University, 3508 TA Utrecht, Netherlands

(Received 25 July 2016; revised manuscript received 24 November 2016; published 11 January 2017)

We investigated thermally activated ionization and thermally activated crossover as the two possibilities of quenching of $5d$ luminescence in Pr^{3+} -doped $\text{Y}_3\text{Al}_{5-x}\text{Ga}_x\text{O}_{12}$. Varying the Ga content x gives the control over the relative energy level location of the $5d$ and $4f^2 : ^3P_J$ states of Pr^{3+} and the host conduction band (CB). Temperature-dependent luminescence lifetime measurements show that the $5d$ luminescence quenching temperature $T_{50\%}$ increases up to $x = 2$ and decreases with further increasing Ga content. This peculiar behavior is explained by a unique transition between the two quenching mechanisms which have an opposite dependence of thermal quenching on Ga content. For low Ga content, thermally activated crossover from the $4f5d$ state to the $4f^2(^3P_J)$ states is the operative quenching mechanism. With increasing Ga content, the activation energy for thermally activated crossover becomes larger, as derived from the configuration coordinate diagram, while from the vacuum referred binding energy diagram the activation energy of thermal ionization becomes smaller. Based on these results, we demonstrated that the thermal quenching of $\text{Pr}^{3+} : 5d_1$ - $4f$ luminescence in $\text{Y}_3\text{Al}_{5-x}\text{Ga}_x\text{O}_{12}$ with $x = 0, 1, 2$ is a thermally activated crossover while for $x = 3, 4, 5$ it results from the thermal ionization.

DOI: [10.1103/PhysRevB.95.014303](https://doi.org/10.1103/PhysRevB.95.014303)

I. INTRODUCTION

The $5d$ - $4f$ luminescence of lanthanide ions Ce^{3+} , Pr^{3+} , Eu^{2+} , and Yb^{2+} has attracted a great deal of attention. The luminescence is crucial in optical applications such as white LEDs, fluorescent tubes, displays, afterglow materials, anticounterfeiting, and scintillators because of their intense broad absorption, high quantum efficiency, fast decay lifetime, and tenability of luminescence colors. For the optical devices based on the $5d$ - $4f$ luminescence, especially the high-power white LEDs, the thermal quenching of the luminescence becomes a problem. Up until about the 1990s, the luminescence quenching of the $5d$ - $4f$ transition was mainly explained by the thermally activated crossover quenching using configuration coordinate (CC) diagrams [1]. However, in the 1990s, Yen *et al.* demonstrated the existence of thermally activated ionization (thermal ionization) quenching from the $\text{Ce}^{3+} : 5d$ excited level in some compounds by photoconductivity analysis [2]. Since then both mechanisms are often discussed as being responsible for thermal quenching of luminescence in white LEDs phosphors [3–7]. However, the mechanism proposed is not always supported by the experimental results. To design new phosphors with $5d$ - $4f$ luminescence and to improve the thermal quenching behavior, it is necessary to elucidate which luminescence quenching process is dominant in the different phosphors.

To understand the two quenching processes, a schematic diagram combining the CC diagram and the vacuum referred binding energy (VRBE) diagram for $\text{Y}_3\text{Al}_5\text{O}_{12}$ (YAG) doped with Ce^{3+} and Pr^{3+} are shown in Fig. 1. Note that the x axis

of the parabolas in the CC diagram is the distance between Ln^{3+} and the coordinating anions (ligands) with a minimum energy of the parabolas for the equilibrium distance. However, the x axis is not shown in this figure. A band diagram is a one-electron energy diagram and relaxation processes involved in optical excitation and emission cannot be included. This incompatibility of band diagrams and configurational coordinate diagrams can be the cause of misunderstanding.

Thermally activated crossover, as shown by the pink arrows in the CC diagram of Fig. 1, is the nonradiative relaxation process from the excited $5d$ potential curve to the lower $4f$ potential curve through the crossing point. At the crossing point, the energy of the $5d$ vibronic state coupling with a few phonons matches that of a higher $4f$ vibronic state and the resonant transition to the $4f$ state is followed by rapid nonradiative relaxation to lower vibronic $4f$ states. The high $4f$ vibrational levels involved have their amplitude concentrated almost exclusively at the extremes (turning points) of the parabola. Thus the thermally activated crossover is often depicted as a thermally activated process with the energy difference between the lowest vibrational level of the excited state and the crossing point of the parabola as activation energy. This activation barrier decreases for a larger parabola offset and a smaller energy difference between the states. Thermal ionization is the thermally activated electron transfer process from the $5d$ state to the conduction band (CB), as shown by the red arrows in Fig. 1. Note that not all the ionized electrons recombine with the photo-oxidized luminescent center nonradiatively. Some of the ionized electrons can transfer back to the $5d$ excited state immediately or after trapping to intrinsic defects and detrapping processes (persistent luminescence and delayed recombination luminescence) [8,9]. In any cases, thermally activated photoionization leads to a reduced light output. The

*ueda.jumpei.5r@kyoto-u.ac.jp

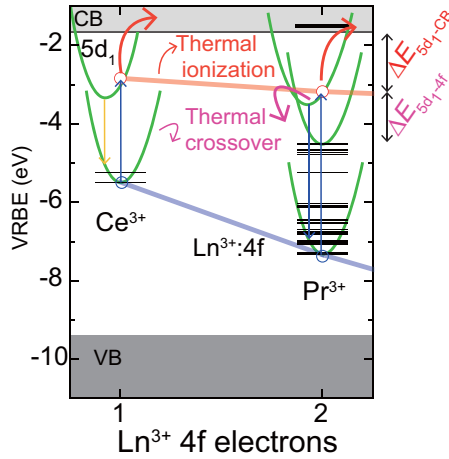


FIG. 1. Schematic diagram combining configuration coordinate (CC) and VRBE diagrams for YAG:Ce³⁺ and YAG:Pr³⁺ explaining thermal quenching of luminescence.

quenching temperature is determined by the energy difference between the emitting excited state and the conduction band edge.

To provide a better understanding of the quenching processes of the $5d$ - $4f$ luminescence, the family of garnet $\text{Ln}_3\text{M}_5\text{O}_{12}$ ($\text{Ln} = \text{Gd}, \text{Y}, \text{Lu}$; $\text{M} = \text{Sc}, \text{Al}, \text{Ga}$) doped with Ce³⁺ and Pr³⁺ serve as important model systems because of the possibility to tune optical properties as a function of covalency, size of the cation site, bandgap, vibrational energies, etc., by variation of the ions on the three different cation sites in the garnet hosts [5,10–13]. In the past, we have focused on the garnet materials doped with Ce³⁺ for the analysis of the quenching mechanisms and for the development of persistent phosphors [14–17]. By performing photoconductivity and thermoluminescence (TL) measurements as a function of temperature and excitation wavelength, we demonstrated that the Ce³⁺ : $5d$ - $4f$ luminescence quenching in $\text{Y}_3\text{Al}_5\text{O}_{12}$, $\text{Y}_3\text{Al}_2\text{Ga}_3\text{O}_{12}$, and $\text{Y}_3\text{Ga}_5\text{O}_{12}$ (YGG) is caused by the ionization process and not by the crossover [14,18,19]. For Pr³⁺-doped YAG and $\text{Lu}_3\text{Al}_5\text{O}_{12}$ (LuAG), precise configuration coordinate diagrams were constructed from low-temperature spectroscopy data and the $5d$ - $4f$ thermal quenching behavior was related to the energy gap between the lowest $5d_1$ state and the next lower $4f$ state [10]. On the basis of the good agreement between the configuration coordinate diagrams and the quenching temperature, the quenching process of the $5d$ - $4f$ luminescence in these materials is attributed to the thermally activated crossover process [10]. Hence, YAG:Pr³⁺ shows thermally activated crossover quenching while YAG:Ce³⁺ is characterized by the thermal ionization quenching. This difference can be understood from the energy diagram of YAG:Pr³⁺ and YAG:Ce³⁺ in Fig. 1. The energy gap between the lowest $5d_1$ state and the CB ($\Delta E_{5d_1\text{-CB}}$) in YAG:Ce and YAG:Pr are 1.4 and 1.1 eV, respectively. On the other hand, the activation energy of thermally activated crossover in YAG:Pr and YAG:Ce is regarded to be totally different because the energy gaps between the $5d_1$ state and the next lower $4f$ level ($\Delta E_{5d_1\text{-}4f}$) are 3.1 eV for Ce³⁺ and 1.7 eV for Pr³⁺. Based on the much smaller gap for Pr³⁺,

thermally activated crossover quenching is expected to start at a much lower temperature.

In this study, to investigate the difference in the quenching process between Ce³⁺ and Pr³⁺, we focus on the optical properties and thermal quenching of $\text{Y}_3\text{Al}_{5-x}\text{Ga}_x\text{O}_{12}$ (YAGG):Pr³⁺. In YAGG:Pr³⁺, it is predicted that $\Delta E_{5d_1\text{-CB}}$ decreases dramatically with increasing Ga content, as was the case for YAGG:Ce³⁺ in our previous paper [18,20]. However, the $\Delta E_{5d_1\text{-}4f}$ is expected to not vary as strongly compared with $\Delta E_{5d_1\text{-CB}}$ since the $4f$ level is not sensitive to the environment around a lanthanide ion and the energy shift of the $5d$ level is much smaller than the conduction-band energy shift in YAGG:Pr³⁺. Consequently, the quenching process of Pr³⁺ : $5d_1$ - $4f$ luminescence in the YAGG host is expected to change with increasing Ga content from the thermally activated crossover to the thermal ionization at the point that the activation energy of thermal ionization becomes much smaller than that of thermally activated crossover. On the basis of experimental results on the luminescence quenching behavior of the YAGG:Pr³⁺ and precise CC diagrams constructed using low-temperature spectroscopy, thermoluminescence excitation (TLE) analysis, and VRBE diagrams, we demonstrated that the quenching of Pr³⁺ : $5d_1$ - $4f$ luminescence in the $x = 0, 1, 2$ samples is thermally activated crossover and that in the $x = 3, 4, 5$ samples is the thermal ionization.

II. EXPERIMENTAL PROCEDURE

For the synthesis of polycrystalline ceramics of $\text{Y}_3\text{Al}_{5-x}\text{Ga}_x\text{O}_{12} : \text{Pr}^{3+}$ (0.2% at the Y site), $\text{Y}_2\text{O}_3 : \text{Pr}^{3+}$ (0.2%) and Ga_2O_3 fine powder prepared using the coprecipitation method and commercial Al_2O_3 (4 N) fine powder were used as starting materials. The stoichiometric amounts of Y_2O_3 (4 N) and Pr_6O_{11} (4 N) powder mixture for $\text{Y}_2\text{O}_3 : \text{Pr}^{3+}$ (0.2%) were dissolved in a mixture of hydrochloric acid and nitric acid, and then Y³⁺ and Pr³⁺ cation solutions (~ 0.4 M) were prepared. After adding a 30-mL cation solution with a 150-mL ammonium hydrogen carbonate (AHC) solution (1 M), precipitate was formed. For Ga_2O_3 , a 30-mL $\text{Ga}(\text{NO}_3)_3$ solution (~ 0.4 M) was added to a 150-mL AHC solution, and then precipitate was formed. Both precipitates were centrifuged and washed three times with deionized water, and then dried and heat-treated at 700 °C for 4 h. Finally, $\text{Y}_2\text{O}_3 : \text{Pr}^{3+}$ (0.2%) and Ga_2O_3 fine powder were obtained. The stoichiometric amounts of powders ($\text{Y}_2\text{O}_3 : \text{Pr}^{3+}$, Ga_2O_3 , Al_2O_3) for $\text{Y}_3\text{Al}_{5-x}\text{Ga}_x\text{O}_{12} : \text{Pr}^{3+}$ (0.2% at the Y site) were mixed in an alumina mortar with ethanol. The obtained slurry was dried, pulverized, and sintered two times at 1500 °C for 6 h in N_2 . The YAG:Ce³⁺ (0.1%) sample was prepared by solid-state reaction at 1600 °C using CeO_2 , Y_2O_3 , and Al_2O_3 chemicals. The crystal phase was identified as a single phase of the garnet structure using an x-ray powder diffraction measurement system (see Fig. S1 in the Supplemental Material [21]). Photoluminescence (PL) and PL excitation (PLE) spectra were measured by detecting emission using a monochromator (Princeton Instruments, Acton SP 2300) and a photomultiplier tube (Hamamatsu, H10330A-75). For excitation either a Xe lamp (Newport, 66921) and a monochromator (Horiba Jobin Yvon, GEMINI180) or a D₂

lamp (Hamamatsu Photonics, L1835) and a monochromator (Acton Research Corporation, VM 502) was used. To control temperature, a closed-cycle He cryostat (SHI-APD, DE-204SLFF) was used. For high-resolution VUV spectroscopy, the beam line BL3B of the UVSOR facility at the Institute for Molecular Science, Okazaki, was used. Emission spectra were detected using a combined spectroscopy system of a grating monochromator (Princeton Instruments, Acton SP 2300i) and a CCD detector (Roper Scientific, LN/CCD-100EB-GI). The excitation spectra were measured with a photomultiplier tube (Hamamatsu, R928) attached at another output port of the grating monochromator.

For the temperature dependence of decay curve measurements, decay curves were recorded using a time-correlated single-photon counting (TCSPC) method under excitation with a 270-nm PLS-270 LED ($\lambda_{ex} = 270$ nm, pulse width ~ 200 ps) and using the detection system of an Edinburgh Instruments FLS920 fluorescence spectrometer with a cooled single-photon counting photomultiplier (Hamamatsu R928P) and an Oxford Instruments liquid helium flow cryostat.

For the thermoluminescence excitation spectra, the samples were illuminated with monochromatic light obtained from a Xe lamp (Newport, 66921) and a monochromator (Newport, 74004), and after the illumination phase the thermoluminescence glow curve was measured using a RISØ TL/OSL reader model DA-15 and a controller model DA-20. The TL was detected with a photomultiplier tube (EMI, 9635QA) filtered by UG-11 (transmittance window from 250 nm to 400 nm).

III. RESULTS AND DISCUSSION

A. Photoluminescence

To illustrate the luminescence behavior of Ce^{3+} and Pr^{3+} in the garnets, Fig. 2 shows the PL and PLE spectra of $Y_3Al_5O_{12}$ doped with Ce^{3+} and Pr^{3+} . In the PL of $YAG:Ce^{3+}$, broad PL bands are observed at around 540 nm which are attributed to the transitions of Ce^{3+} from $4f^05d^1$ to $4f^1(2F_{5/2}$ and $2F_{7/2})$. In the

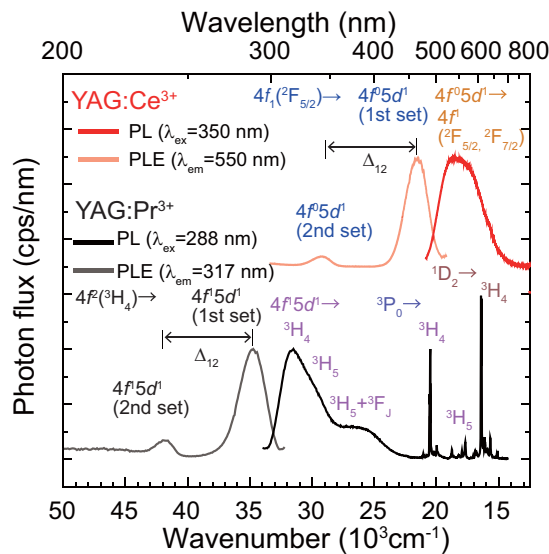


FIG. 2. PL and PLE in $Y_3Al_5O_{12}$ doped with 0.2% Pr^{3+} and 0.1% Ce^{3+} .

PLE of $YAG:Ce^{3+}$, two PLE bands were observed at 460 nm and 340 nm. These two bands are attributed to the $4f^05d^1$ states split by the crystal field. In the PL of $YAG:Pr^{3+}$, broad PL bands are observed at around 300, 320, and 360 nm, which are attributed to the transition of Pr^{3+} from the $4f^15d^1$ state to the $4f^2(3H_4, 3H_5, 3H_6 + 3F_J)$ states, respectively. In addition to broad PL bands, sharp PL peaks attributed to the $Pr^{3+}: 3P_0 \rightarrow 3H_J, 3F_J$ and $1D_2 \rightarrow 3H_4$ $f-f$ transitions are observed. In the PLE of the $4f^15d^1 \rightarrow 4f^2(3H_4)$ luminescence at 303 nm in $YAG:Pr^{3+}$, two broad PLE bands are observed at around 280 and 240 nm, which are attributed to the transitions of Pr^{3+} from $4f^2(3H_4)$ to the first and second sets of $4f^15d^1$ excitation bands, respectively. Pr^{3+} includes the energetic 140 states of the $4f^15d^1$ configuration. Therefore, it is difficult to assign all of the levels in the PLE spectrum of $YAG:Pr^{3+}$. However, compared with the $4f^05d^1$ PLE bands of Ce^{3+} -doped YAG, which is split by the crystal field term as shown in Fig. 2, $YAG:Pr^{3+}$ shows similar PLE bands. The energy differences (Δ_{12}) between the first and second set of PLE bands related $5d$ in $YAG:Ce^{3+}$ and $YAG:Pr^{3+}$ are 7641 and 7058 cm^{-1} , respectively, at ambient temperature. From these results, the first and second set of $4f^15d^1$ PLE bands in $YAG:Pr^{3+}$ would be split mainly by the crystal field but not by the spin-orbit coupling.

Figure 3 shows an overview of the PL and PLE spectra of $Y_3Al_{5-x}Ga_xO_{12} : Pr^{3+}$ ($x = 0, 1, 2, 3, 4$) at 10 K. All samples show the typical $5d-4f$ transitions of Pr^{3+} in both PL and PLE, similar to those shown in Fig. 2. When the Ga content increases in the host composition, the $Pr^{3+} : 4f^15d^1$ (first set)- $4f^2(3H_4)$ PL and PLE bands are shifted to higher energy. For the second set of $4f^15d^1$, the band is shifted to lower energies with increasing Ga content. The decrease of Δ_{12}

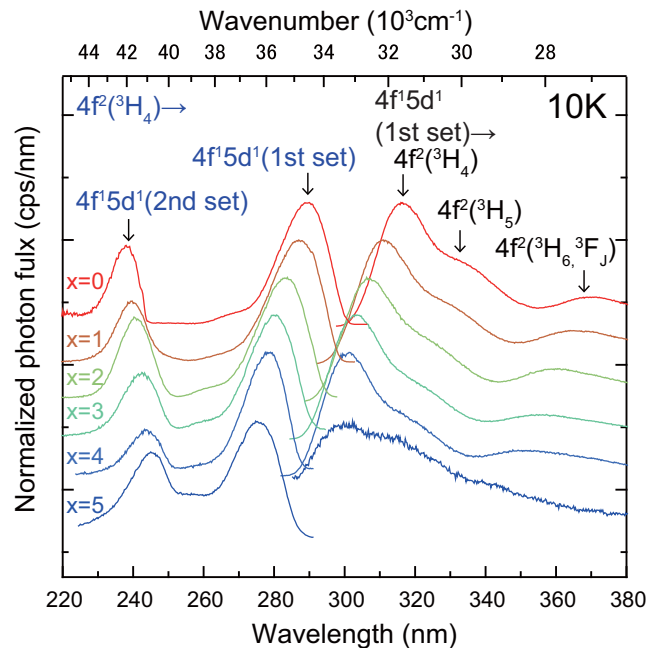


FIG. 3. PL (for excitation to the $5d_1$ state) and PLE (for $5d_1-4f$ luminescence) of $Y_3Al_{5-x}Ga_xO_{12} : 0.2\%Pr^{3+}$ ($x = 0, 1, 2, 3, 4$) at 10 K. For the $x = 5$ samples, PLE was measured by monitoring $3P_J$ luminescence.

TABLE I. The parameters obtained for $Y_3Al_{5-x}Ga_xO_{12} : Pr^{3+}$ from the PL/PLE spectra and temperature dependence of PL intensity. $5d_1-4f^2(^3H_4)$ emission peak (E_{5d_1Em}), $4f^2-5d_1$ and $5d_2$ excitation peaks (E_{5d_1Ex} , E_{5d_2Ex}). Stokes shift (SS), energy gap between $5d_1$ and the crossing point with the next lower $4f$ level (ΔE_{5d_1-CP}), and from temperature-dependent luminescence decay measurements: quenching temperature ($T_{50\%}$), radiative rate (Γ_v), attempt rate of nonradiative process (Γ_0), and activation energy of thermal quenching (ΔE_{TQ}).

x	E_{5d_1Em} (cm^{-1})	E_{5d_1Ex} (cm^{-1})	E_{5d_2Ex} (cm^{-1})	SS (cm^{-1})	ΔE_{5d_1-CP} (cm^{-1})	$T_{50\%}$ (K)	Γ_v ($10^7 s^{-1}$)	Γ_0 ($10^9 s^{-1}$)	ΔE_{TQ} (eV)
0	31646	34542	42017	2896	17388	321	4.63	31.3	0.17
1	32154	34843	41754	2689	18487	377	5.04	46.7	0.21
2	32600	35335	41580	2735	19839	407	5.70	305	0.29
3	32949	35747	41237	2798	20713	316	6.26	59.6	0.18
4	33195	35939	41109	2744	22097	173	7.77	7.97	0.07
5	33384	36331	40816	2947	20857	149	10.2	5.05	0.05

with increasing Ga content is analogous to the Ga content dependence of Δ_{12} observed for Ce^{3+} in $Y_3Al_{5-x}Ga_xO_{12}$ [18,20]. The data obtained for the $4f^15d^1-4f^2$ PL peak energy (E_{5d_1Em}) and the first and second sets of $4f^15d^1$ PLE peak energies (E_{5d_1Ex} and E_{5d_2Ex}) are listed in columns 2, 3, and 4 in Table I. The Stokes shift energy (SS) was estimated by subtracting E_{5d_1Em} from E_{5d_1Ex} and is shown in column 5 of Table I.

B. Zero phonon line, phonon progression, and Huang-Rhys parameter

To be able to construct a reliable configurational coordinate diagram and estimate the Huang-Rhys coupling parameter, high-resolution spectra recorded at low temperature are required for samples with low dopant concentrations to prevent inhomogeneous broadening by dopant disorder, spectral shifts because of reabsorption, and saturation effects [3]. Figure 4

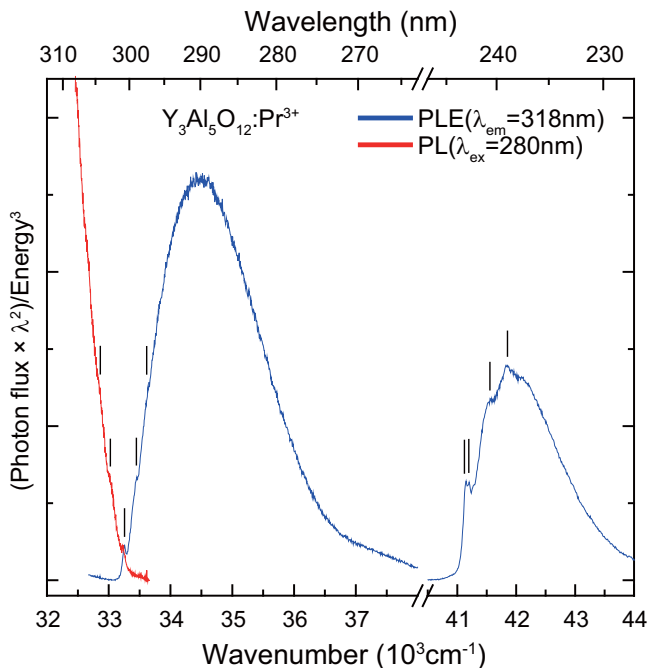


FIG. 4. High-resolution PL spectrum (excited by 280 nm) and PLE spectrum (of 318 nm luminescence) in $YAG:0.2\%Pr^{3+}$ at 8 K. Vertical black lines are phonon lines.

shows the high-resolution PL and PLE spectra at 8 K in $YAG:0.2\%Pr^{3+}$. The luminescence spectra of $YAG:0.2\%Pr^{3+}$ shows a zero phonon line (ZPL) at $33\,257\,cm^{-1}$ and vibronic progression in both PL and PLE spectra, while other $YAGG:Pr^{3+}$ samples with different Ga content do not. The absence of fine structure can be explained by the fact that PL and PLE bands of $YAGG:Pr^{3+}$ are affected by inhomogeneous broadening which originates from the local environment around Pr^{3+} with statistically varying number of Al and Ga in the nearest octahedral and tetrahedral sites. For the transitions between $4f^2(^3H_4)$ and $4f^15d^1$ in the high-resolution PLE and PL of $YAG:Pr^{3+}$, the typical mirror symmetry is observed. Similar mirror symmetry for $YAG:Pr^{3+}$ was reported by before [10]. The typical mirror symmetry is one of the evidences of phonon sidebands. The positions of the ZPLs in the PL and PLE spectra have a small difference of $28\,cm^{-1}$, possibly because of a small redshift of ZPL in the PL spectrum by reabsorption [22]. Alternatively, the small offset may be result of a small calibration error. In the PLE spectrum, the zero-phonon line at $33\,257\,cm^{-1}$ and two vibronic lines at 199 and $391\,cm^{-1}$ higher energy are observed. The vibronic lines are assigned to a one- and two-phonon replica indicating that the $f-d$ transition strongly couples with approximately $196\,cm^{-1}$ vibration modes. For the transitions between $4f^1(^2F_{5/2})$ and $5d_1$ in $YAG:Ce$, coupling to similar vibrational modes of $200\,cm^{-1}$ was reported [3]. Because the vibrational energy in the same host material does not depend on the type of (Ln) dopant ion according to the experimental results and theoretical calculation [23], the $196\,cm^{-1}$ vibration mode found in $YAG:Pr^{3+}$ is in agreement with what is expected.

From these, the Huang-Rhys electron-phonon coupling parameter (S) can be obtained using the relationship of $I_{ZPL} = I_0 \times \exp(-S)$, where I_{ZPL} and I_0 are the intensity of ZPL and total emission intensity, respectively [3,24]. This method can be valid even though there are 140 states of $4f^15d^1$ configuration. This is because only the lowest $4f^15d^1$ level can be populated at 8 K, and other energy levels can be ignored for the luminescence. The Huang-Rhys parameters obtained is 5.5. The Huang-Rhys parameter reflects the change in bond length for a transition between two states. According to the similar vibrational mode in PL and PLE spectra as shown in Fig. 4, we can assume the $5d$ and $4f$ states as having the same force constant for the CC diagram. This assumption is reasonable because the force constant can be expressed by $k = \mu\omega^2$, where μ is the reduced mass of the vibration and ω

is the vibrational frequency, and these parameters are common to both ground and excited vibrational coordinates in the same host [25,26].

C. Configuration coordinate (CC) diagram

On the basis of the obtained energies from the low-temperature spectroscopy, the configuration coordinate diagram of YAG:Pr³⁺ was constructed as shown in Fig. 5(a) by using Eqs. (1)–(4):

$$E_{5d_1}(x) = E_{z_{p,4f-5d_1}} + S\hbar\omega\left(\frac{x}{a} - 1\right)^2, \quad (1)$$

$$E_{3H_4}(x) = S\hbar\omega\left(\frac{x}{a}\right)^2, \quad (2)$$

$$E_{3P_2}(x) = E_{3P_{2Ex}} + S\hbar\omega\left(\frac{x}{a}\right)^2, \quad (3)$$

$$S\hbar\omega = \frac{SS}{2}, \quad (4)$$

$$E_{z_{p,4f-5d_1}} = E_{5d_1Ex} - \frac{SS}{2}, \quad (5)$$

where $E_{5d_1}(x)$, $E_{3H_4}(x)$, and $E_{3P_2}(x)$ are the potential curves of the first set of $4f^15d^1$, the 3H_4 ground state, and 3P_2 excited state of $4f^1$ as a function of equilibrium internuclear distance x , $E_{z_{p,4f-5d_1}}$ is the ZPL energy of the $4f-4f^15d^1$ transition, $E_{3P_{2Ex}}$ is the excitation peak of the 3P_2 level, E_{5d_1Ex} is the excitation peak energy of the first set of $4f^15d^1$, S is the Huang-Rhys parameter, $\hbar\omega$ is the vibrational energy, SS is the Stokes shift energy, and a is the configuration offset of the $5d$ potential curve from the bottom of the $4f$ potential curve (taken as zero), as shown in Fig. 5(a) [1]. Here, we assumed that the $4f$ and $4f^15d^1$ parabola have equal force constants. For a Huang-Rhys coupling parameter

of ~ 5 , intermediate coupling, this is a valid assumption. In this case, the Stokes shift is composed of the same phonon relaxation energies in the $4f^15d^1$ and $4f^1$ state and Eq. (4) can be obtained. Because of the difference in excitation peak energy E_{5d_1Ex} and ZPL energy $E_{z_{p,4f-5d_1}}$ being equal to half of the Stokes shift energy, Eq. (5) is also obtained. The CC diagrams of other YAG:Pr systems were constructed based on the above equations and the data are collected in Table I. The enlarged view around the crossing point between the $5d_1$ level and the next lower $4f^2(^3P_2)$ level is shown in Fig. 5(b). To visualize the tendency of activation energy clearly, only the $4f^2(^3P_2)$ level of YAG:Pr³⁺ is drawn in Fig. 5(b) because the difference of 3P_2 energy levels in YAGG:Pr³⁺ is very small. However, for the calculation of activation energy, we used each 3P_2 energy level in each YAGG:Pr³⁺ sample (see Fig. S4 and Table S1 in the Supplemental Material [21]). For increasing Ga content, the energy of the first set of $4f^15d^1$ states is shifted upwards so that the crossing point energy between the first set of $4f^15d^1$ and $4f^2(^3P_2)$ parabolas also increases, as shown in Fig. 5(b). The energy gap (ΔE_{5d_1-CP}) between the bottom of the first set of $4f^15d^1$ parabola and the crossing point was estimated as shown in column 6 of Table I. The ΔE_{5d_1-CP} is overestimated compared with the actual activation energy as shown later, because in actuality the anharmonicities of the potential curve will reduce the energy barrier from the $5d$ state to the crossing point. However, the obtained ΔE_{5d_1-CP} can be compared among the YAGG:Pr samples. The increase in energy gap ΔE_{5d_1-CP} suggests that the quenching temperature increases with Ga content when the quenching process is due to the thermally activated crossover.

D. Temperature quenching behavior

To determine the luminescence quenching temperature the temperature dependence of the lifetime of the Pr³⁺ : $4f^1(^2F_{5/2})5d$ luminescence was investigated as shown in Fig. 6. The lifetimes were estimated by single exponential fitting to luminescence decay curves (see Figs. S2 and S3 in the Supplemental Material [21]). In previous work it was shown that the most accurate way to determine the luminescence quenching temperatures for YAG:Ce was to measure lifetimes for materials with very low dopant concentrations [23] rather than relying on intensity measurements, which can be influenced by changes in absorption strength with temperature, or using higher dopant concentrations where thermally activated concentration quenching obscures the observation of quenching of the emitting center [3]. At 4.2 K, the lifetime decreases with increasing Ga content. An increase in refractive index with increasing Ga content can explain this trend. The lifetime of the Pr³⁺ luminescence of all samples decreases with increasing temperature, and all samples show that luminescence becomes quenched below 500 K. From the lifetime data, the quenching temperature $T_{50\%}$, which is the temperature at which the lifetime becomes 50% of that at low temperatures, was estimated as shown in column 7 of Table I. $T_{50\%}$ increases up to $x = 2$ and then decreases for higher Ga content. This behavior corresponds to the prediction from the configuration coordinate diagram for the samples with $x = 0, 1$, and 2 as shown in Fig. 5(b), but it is not in agreement with the results of the CC diagram for $x = 3, 4$,

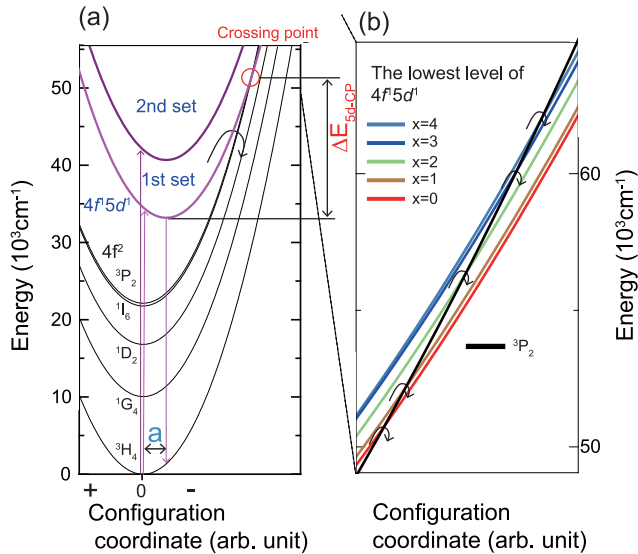


FIG. 5. (a) Configuration coordinate diagram showing the various $4f^2$ and $4f^15d^1$ states of Pr³⁺ in YAG:Pr³⁺ and (b) enlarged view of the CC diagram around the crossing point of the lowest energy $4f^15d^1$ state with the highest energy $4f^2$ states (3P_2) for Y₃Al_{5-x}Ga_xO₁₂: Pr³⁺ ($x = 0-4$).

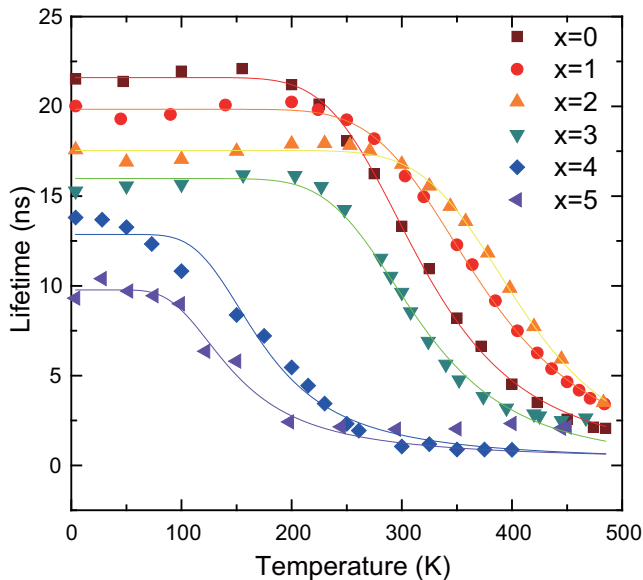


FIG. 6. Temperature dependence of lifetime in $Y_3Al_{5-x}Ga_xO_{12} : Pr^{3+}$.

and 5. This result suggests that for samples with $x = 3, 4,$ and 5 another mechanism is responsible for the luminescence quenching. As discussed above, this can be expected, as the first set of $4f^15d^1$ states moves up in energy for increasing x while the CB edge moves down in energy, thus making the energy barrier for thermal ionization from the $5d$ state to the CB smaller. These observations show that between $x = 2$ and $x = 3$ there is a transition from temperature quenching by crossover to the $4f^2(^3P_2)$ parabola in the CC diagram to photoionization to the conduction band.

To further the quantitative explanation for the peculiar trend in the quenching temperatures observed for the $Pr^{3+}d-f$ luminescence in $Y_3Al_{5-x}Ga_xO_{12} : Pr^{3+}$ ($x = 0-5$) with x , activation energies, radiative rate, and attempt rate of the non-radiative process are derived from the temperature dependence of lifetime according to the single barrier quenching model, Eq. (6):

$$\tau(T) = \frac{1}{\Gamma_v + \Gamma_0 \exp(-\Delta E_{TQ}/kT)}, \quad (6)$$

where τ is the lifetime, Γ_v is the radiative rate, Γ_0 is the attempt rate of the nonradiative process, ΔE_{TQ} is the activation energy, k is the Boltzmann constant, and T is the temperature. Here, we applied the equation of one barrier quenching process despite the possibility of two quenching processes. This is because if the activation energy of one nonradiative process is smaller than that of another, the quenching curve mainly depends on the parameters of the nonradiative with the smaller activation energy. The fitting by one barrier quenching process is a reasonable method to obtain the activation energy of the quenching process (see Fig. S5 and Table S2 in the Supplemental Material [21]).

The parameters obtained for Γ_v , Γ_0 , and ΔE_{TQ} are listed in columns 8, 9, and 10 of Table I. For comparison with ΔE_{TQ} in other Pr^{3+} -doped compounds exploited in the scintillator area, the unit of ΔE_{TQ} is reported in electronvolts [27,28].

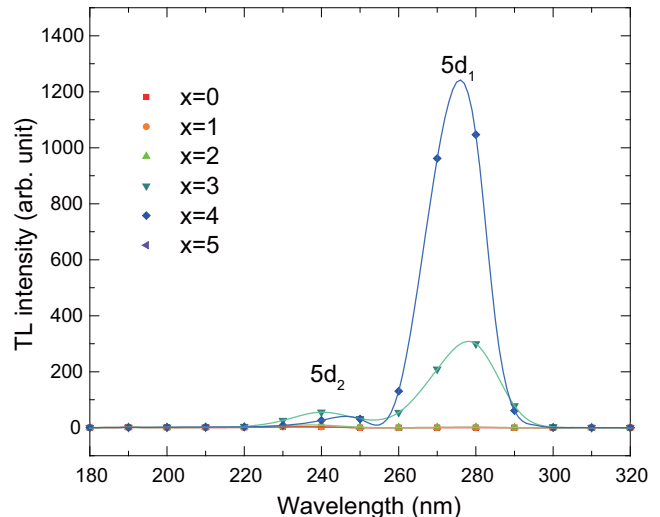


FIG. 7. Integrated TL intensity between 300 K and 600 K as a function of charging excitation wavelength from 180 nm to 320 nm with 300 s charging time in $Y_3Al_{5-x}Ga_xO_{12} : Pr^{3+}$.

ΔE_{TQ} increases up to $x = 2$ and then decreases with increasing Ga content, following the same tendency of the Ga content dependence of quenching temperature.

E. TLE analysis

To provide further insight into the quenching process, thermoluminescence excitation spectra were measured. TLE spectroscopy is a powerful tool to investigate whether thermal ionization from the excited $5d$ state occurs [18,19,29]. The observation of a peak in a TL glow curve is a direct evidence of thermal ionization, because the trap filling from the excited state proceeds by electron transport to the conduction band and trapping of the conduction-band electrons. As a result, the observation of thermoluminescence after excitation to the $5d_1$ state in the temperature range where luminescence quenching is observed provides a clear signature of thermal ionization. The thermal quenching for the $d-f$ luminescence in all $Y_3Al_{5-x}Ga_xO_{12} : Pr^{3+}$ ($x = 0-5$) samples starts to occur below 300 K, as shown in Fig. 6. Therefore, thermoluminescence glow curves in the range between 300 and 600 K after charging at 300 K were measured (see Fig. S6 in the Supplemental Material [21]). In addition, the integrated intensity of TL glow peaks was plotted as a function of charging wavelength, which is TLE spectrum (see Fig. S7 in the Supplemental Material [21]). In the TLE spectra of Fig. 7, only $x = 3$ and $x = 4$ samples show a strong TLE band at 275 nm, which is attributed to the $Pr^{3+} : 4f-5d_1$ transition. This observation confirms that for the $x = 3$ and $x = 4$ samples the quenching mechanism is thermal ionization from the $5d_1$ to the conduction band.

F. VRBE diagram

We also tried to elucidate the quenching processes considering a different approach, i.e., by means of the vacuum referred binding energy diagram, which is a helpful tool to estimate the energy gap between $5d_1$ and the conduction band. First, the band-gap energies of $Y_3Al_{5-x}Ga_xO_{12} : Pr^{3+}$ were analyzed

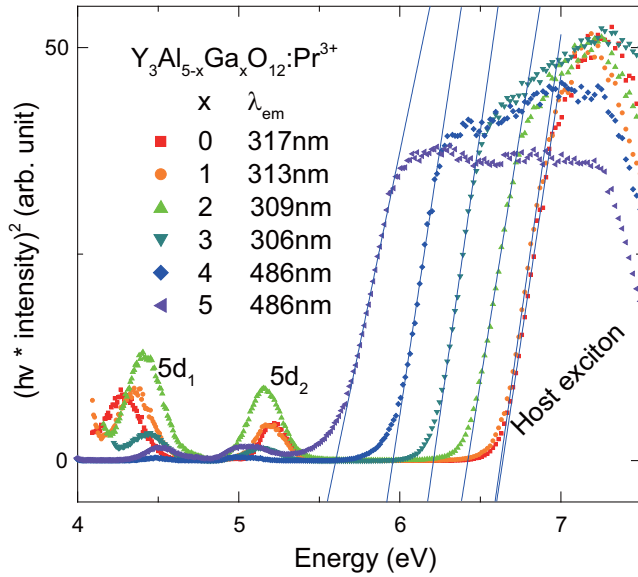


FIG. 8. Tauc plot of PLE spectra in the VUV region in $Y_3Al_{5-x}Ga_xO_{12} : Pr^{3+}$.

from the PLE spectra in the VUV region as shown in Fig. 8. (The data related to VRBE diagrams are in electronvolt units according to the conventional VRBE diagram [20,30,31].) For the PLE spectra of the samples from $x = 0$ to $x = 3$, the $5d_1-4f$ transition was monitored. Because of the weak luminescence efficiency of the $5d_1-4f$ transition for $x = 4$ and 5 , the ${}^3P_0-{}^3H_4$ transition was monitored instead. In the PLE in the VUV region for all samples, the excitation band due to the host exciton was observed from 5.5 to 7 eV. Beyond the absorption edges at higher energy, the excitation is saturated. The energy of the fundamental absorption edge decreases with increasing Ga content. Using a Tauc plot of the direct allowed transition, the fundamental absorption energies were estimated [32]. The host exciton energy E^{ex} was estimated by adding the similar calibration value of 0.46 eV to fundamental absorption, as in our previous paper [18] and shown in column 2 of Table II. The obtained E^{ex} is in good agreement with the reported E^{ex} in $Y_3Al_{5-x}Ga_xO_{12} : Ce^{3+}$ [18,20]. The stacked VRBE diagrams were constructed mainly using the E^{CT} parameters (charge transfer energy of Eu^{3+}) from the data reported by Jia *et al.* [33] and $U(6,A)$ (energy difference between Eu^{2+} and Eu^{3+}) reported by Dorenbos [34], as shown in columns 3 and 4 of Table II. For the $5d_1$ and $5d_2$ energies of the Pr^{3+} -doped YAGG

TABLE II. Experimental data on exciton energy (E^{ex}), charge transfer (E^{CT}) and Coulomb repulsion energy [$U(6, A)$], and ΔE_{5d_1-CB} for $Y_3Al_{5-x}Ga_xO_{12} : Pr^{3+}$.

x	E^{ex} (eV)	E^{CT} (eV)	$U(6,A)$ (eV)	ΔE_{5d_1-CB} (eV)
0	7.10	5.42 [33]	6.79 [34]	1.41
1	7.09	5.34 [18]	6.79 [34]	1.37
2	6.88	5.25 [33]	6.79 [34]	1.18
3	6.67	5.19 [33]	6.79 [34]	0.96
4	6.42	5.12 [33]	6.79 [34]	0.74
5	6.06	5.05 [33]	6.79 [34]	0.37

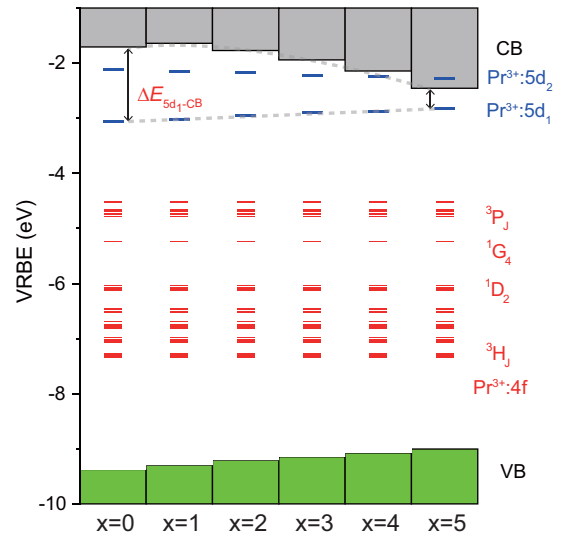


FIG. 9. Stacked VRBE diagram of $Y_3Al_{5-x}Ga_xO_{12} : Pr^{3+}$.

system as shown in Fig. 9, the band maxima from this work were used. The energy gap between $5d_1$ and the bottom of the CB (ΔE_{5d_1-CB}) was estimated from the VRBE diagram as shown in column 5 of Table II. ΔE_{5d_1-CB} drops significantly from $x = 3$ with increasing Ga content. This tendency is consistent with the Ga content dependence of the activation energy ΔE_{TQ} and decrease in quenching temperature $T_{50\%}$ above $x = 3$. The VRBE diagram strongly supports that the quenching processes for $x = 0, 1$, and 2 samples and for $x = 3, 4$, and 5 are caused by thermally activated crossover and thermal ionization, respectively.

IV. CONCLUSIONS

High-resolution PL and PLE spectra of YAG:Pr³⁺ were measured at 8 K. The energy of the ZPL (zero phonon line) is estimated to be $33\,257\text{ cm}^{-1}$ and the vibronic energy is 196 cm^{-1} . The estimated electron-lattice coupling Huang-Rhys parameter for the $5d$ and $4f$ states of Pr^{3+} are 5.5 as derived from the intensity ratio of ZPL and total transition. From low-temperature spectroscopy, the configuration coordinate diagrams of $Y_3Al_{5-x}Ga_xO_{12} : Pr^{3+}$ were constructed. From those CC diagrams, the activation energy of thermally activated crossover was found to increase with increasing Ga content. However, from the temperature dependence of the lifetime of the $Pr^{3+} : 5d_1$ level the quenching temperature ($T_{50\%}$) increases up to $x = 2$ and decreases with increasing Ga content. From the TLE excitation (TLE) spectra, the $Pr^{3+} : 5d_1$ band (the lowest excited $5d$ level) was observed at around 300 nm in the samples above $x = 3$ Ga content. From the VRBE diagram, the activation energy of thermal ionization decreases with increasing Ga content. Based on the CC diagram, VRBE diagram, and TLE spectra, we demonstrated that the quenching of $Pr^{3+} : 5d_1-4f$ luminescence in $Y_3Al_{5-x}Ga_xO_{12}$ with $x = 0, 1, 2$ is thermally activated crossover and that with $x = 3, 4, 5$ is the thermally activated ionization.

ACKNOWLEDGMENTS

VUV spectroscopy was performed at the UVSOR facility under the Joint Studies Program (28-521) of the Institute

for Molecular Science. We also appreciate Prof. Kitaura at Yamagata University for helping us to measure VUV spectroscopy. This work was supported by JSPS KAKENHI through Grant No. 16K05934.

-
- [1] C. Struck and W. Fonger, *Understanding Luminescence Spectra and Efficiency Using W_p and Related Functions* (Springer, Berlin, 1991), Vol. 13.
- [2] W. M. Yen, M. Raukas, S. A. Basun, W. van Schaik, and U. Happek, *J. Lumin.* **69**, 287 (1996).
- [3] V. Bachmann, C. Ronda, and A. Meijerink, *Chem. Mater.* **21**, 2077 (2009).
- [4] A. A. Setlur, W. J. Heward, Y. Gao, A. M. Srivastava, R. G. Chandran, and M. V. Shankar, *Chem. Mater.* **18**, 3314 (2006).
- [5] J. M. Ogiegłó, A. Katelnikovas, A. Zych, T. Jüstel, A. Meijerink, and C. R. Ronda, *J. Phys. Chem. A* **117**, 2479 (2013).
- [6] J. Zhong, W. Zhuang, X. Xing, R. Liu, Y. Li, Y. Liu, and Y. Hu, *J. Phys. Chem. C* **119**, 5562 (2015).
- [7] C. C. Lin and R.-S. Liu, *J. Phys. Chem. Lett.* **2**, 1268 (2011).
- [8] M. Nikl, A. Vedda, M. Fasoli, I. Fontana, V. V. Laguta, E. Mihokova, J. Pejchal, J. Rosa, and K. Nejezchleb, *Phys. Rev. B* **76**, 195121 (2007).
- [9] E. Mihoková, M. Nikl, J. A. Mareš, A. Beitlerová, A. Vedda, K. Nejezchleb, K. Blažek, and C. D'Ambrosio, *J. Lumin.* **126**, 77 (2007).
- [10] K. V. Ivanovskikh, J. M. Ogiegłó, A. Zych, C. R. Ronda, and A. Meijerink, *ECS J. Solid. State Sci. Technol.* **2**, R3148 (2013).
- [11] J. M. Ogiegłó, A. Zych, T. Jüstel, A. Meijerink, and C. R. Ronda, *Opt. Mater.* **35**, 322 (2013).
- [12] M. Fasoli, A. Vedda, M. Nikl, C. Jiang, B. P. Uberuaga, D. A. Andersson, K. J. McClellan, and C. R. Stanek, *Phys. Rev. B* **84**, 081102 (2011).
- [13] A. Katelnikovas, H. Bettentrup, D. Dutczak, A. Kareiva, and T. Jüstel, *J. Lumin.* **131**, 2754 (2011).
- [14] J. Ueda, S. Tanabe, and T. Nakanishi, *J. Appl. Phys.* **110**, 053102 (2011).
- [15] J. Ueda, K. Aishima, and S. Tanabe, *Opt. Mater.* **35**, 1952 (2013).
- [16] J. Ueda, K. Kuroishi, and S. Tanabe, *Appl. Phys. Lett.* **104**, 101904 (2014).
- [17] J. Ueda, M. Yagi, and S. Tanabe, *ECS J. Solid. State Sci. Technol.* **5**, R219 (2016).
- [18] J. Ueda, P. Dorenbos, A. J. J. Bos, K. Kuroishi, and S. Tanabe, *J. Mater. Chem. C* **3**, 5642 (2015).
- [19] J. Ueda, P. Dorenbos, A. J. J. Bos, A. Meijerink, and S. Tanabe, *J. Phys. Chem. C* **119**, 25003 (2015).
- [20] P. Dorenbos, *J. Lumin.* **134**, 310 (2013).
- [21] See Supplemental Material at <http://link.aps.org/supplemental/10.1103/PhysRevB.95.014303> for additional data: XRD patterns, luminescence decay curves, photoluminescence related to the $4f-4f$ transitions of Pr^{3+} , simulation results of quenching curves, thermoluminescence glow curves, and temperature-charging wavelength contour plot for TL intensity.
- [22] J. M. Ogiegłó, A. Zych, K. V. Ivanovskikh, T. Jüstel, C. R. Ronda, and A. Meijerink, *J. Phys. Chem. A* **116**, 8464 (2012).
- [23] M. de Jong, L. Seijo, A. Meijerink, and F. T. Rabouw, *Phys. Chem. Chem. Phys.* **17**, 16959 (2015).
- [24] B. Henderson and G. F. Imbusch, *Optical Spectroscopy of Inorganic Solids* (Clarendon Press, Oxford, UK, 2006).
- [25] Z. Barandiarán, A. Meijerink, and L. Seijo, *Phys. Chem. Chem. Phys.* **17**, 19874 (2015).
- [26] M. Krośnicki, A. Kędzierski, L. Seijo, and Z. Barandiarán, *J. Phys. Chem. A* **118**, 358 (2014).
- [27] M. Nikl, H. Ogino, A. Yoshikawa, E. Mihokova, J. Pejchal, A. Beitlerova, A. Novoselov, and T. Fukuda, *Chem. Phys. Lett.* **410**, 218 (2005).
- [28] J. Pejchal, M. Nikl, E. Mihokova, A. Novoselov, A. Yoshikawa, and R. T. Williams, *J. Lumin.* **129**, 1857 (2009).
- [29] A. J. J. Bos, R. M. van Duijvenvoorde, E. van der Kolk, W. Drozdowski, and P. Dorenbos, *J. Lumin.* **131**, 1465 (2011).
- [30] P. Dorenbos, *Phys. Rev. B* **87**, 035118 (2013).
- [31] P. Dorenbos, *J. Phys.: Condens. Matter* **25**, 225501 (2013).
- [32] J. Tauc, *Mater. Res. Bull.* **3**, 37 (1968).
- [33] P. Y. Jia, J. Lin, X. M. Han, and M. Yu, *Thin Solid Films* **483**, 122 (2005).
- [34] P. Dorenbos, *J. Lumin.* **135**, 93 (2013).